RESEARCH ARTICLE | NOVEMBER 27 2023

Research on the impact of air-blowing on aerodynamic drag reduction and wake characteristics of a high-speed maglev train ⊘

Zheng-Xin Che (车正鑫) ⓘ ; Zheng-Wei Chen (陈争卫) ✉ ⓘ ; Yi-Qing Ni (倪一清) ⓘ ; Sha Huang (黄莎) ⓘ ;
Zhi-Wei Li (李志伟) ⓘ

Check for updates

View Online

Export Citation

Physics of Fluids

Special Topic:
Selected Papers from the 2023 Non-Newtonian
Fluid Mechanics Symposium in China

Submit Today

AIP Publishing

AIP Publishing
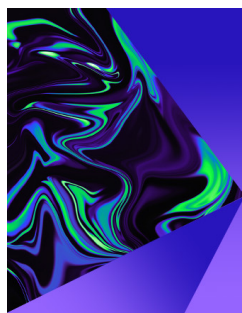
Research on the impact of air-blowing on aerodynamic drag reduction and wake characteristics of a high-speed maglev train Ⓕ

Zheng-Xin Che (车正鑫),[1,2] Ⓘ Zheng-Wei Chen (陈争卫),[1,2,a] Ⓘ Yi-Qing Ni (倪一清),[1,2] Ⓘ Sha Huang (黄莎),[3] Ⓘ and Zhi-Wei Li (李志伟)[3] Ⓘ

AFFILIATIONS

[1]Department of Civil and Environmental Engineering, The Hong Kong Polytechnic University, Hong Kong, People's Republic of China
[2]National Rail Transit Electrification and Automation Engineering Technology Research Center (Hong Kong Branch), Hong Kong, People's Republic of China
[3]School of Rail Transportation, Wuyi University, Jiangmen 529020, China

[a]Author to whom correspondence should be addressed: zhengwei.chen@polyu.edu.hk

ABSTRACT

The maglev train fills the speed gap between ground transportation and airplanes. However, the increasing train speed results in greater energy losses due to increased aerodynamic drag, impeding the green and sustainable development of high-speed railways. This study employs the numerical simulation method to explore the effects of installing air-blowing slots on the surface of the TR08 maglev train's tail car and blowing air along three different directions at two different speeds on drag reduction and the characteristics of the wake flow field. Among them, only blowing air along the streamwise direction at speeds of 12 m/s (X_{12}) and 24 m/s (X_{24}) shows drag reduction effects of 2.06% and 6.53%, respectively. However, considering the energy efficiency, only X_{12} achieves a net energy saving of 58.96%, while the energy consumption by blowing air and saving by reducing drag in X_{24} are roughly balanced. Air-blowing reduces the aerodynamic lift of the tail car (C_l), with blowing air along the perpendicular direction at 24 m/s (Z_{24}) reducing the C_l by 99.57%. Additionally, Z_{24} reduces the maximum velocity value of the train-induced air flow ($\overline{U_{smax}}$) by 61.91%. The research findings provide new insight and data support for the development of blowing/suction drag reduction techniques.

NOMENCLATURE

BOS	the position of the beginning of the air-blowing slots
CM	coarse meshing
FM	fine meshing
H	the height of the train
L	the length of the train
MM	medium meshing
MOS	the middle position of the streamlined train surface
N	case of blowing air in the normal direction of the slots' surface
N_{12}	case of blowing air in the normal direction of the slots' surface at the speed of 12 m/s
N_{24}	case of blowing air in the normal direction of the slots' surface at the speed of 24 m/s
Ori	case of no air-blowing
P1	the tail car's streamlined surface with smaller flow direction component
P2	the tail car's streamlined surface with larger flow direction component
S_{tep}	computational steps
W	the width of the train
W_l	the wake length
W_w	the wake width
X	case of blowing air in the streamwise direction
X_{12}	case of blowing air in the streamwise direction at the speed of 12 m/s
X_{24}	case of blowing air in the streamwise direction at the speed of 24 m/s
Y1	the spanwise position where y = 0
Y2	the spanwise position where $0.28W$ from Y1
Z	case of blowing air in the perpendicular direction

Z1   the vertical position where positive $0.345H$ from the rock bottom of the train
Z2   the vertical position where positive $0.28H$ from Z1
Z3   the vertical position where positive $0.28H$ from Z2
Z_{12} case of blowing air in the perpendicular direction at the speed of 12 m/s
Z_{24} case of blowing air in the perpendicular direction at the speed of 24 m/s

Abbreviations

CFL   Courant–Friedrichs–Lewy number
IDDES   improved delayed detached eddy simulation
PSD   the power spectral density
SIMPLEC   semi-implicit method for pressure linked equations-consistent
SST   shear stress transport

I. INTRODUCTION

Maglev trains have overcome the limitations of wheel-rail adhesion, presenting higher potential for acceleration.[1] The introduction of a 600 km/h maglev train has bridged the speed gap between high-speed trains and airplanes.[2] However, the exponentially increasing aerodynamic drag with the train's operating speed leads to heightened energy consumption,[3] thereby posing a significant obstacle to the green and sustainable development of high-speed railways.

Reducing aerodynamic drag has been a focal point of academic research in high-speed trains. Passive drag reduction methods, such as train shape optimization,[4–8] the addition of flow control devices,[9–12] and surface microstructure treatments,[13–16] have achieved notable drag reduction effects. However, these passive methods have fixed design outcomes and limited drag reduction capabilities, as they cannot adapt in real-time to the train's operating conditions to achieve optimal drag reduction. Active control methods, which have been widely studied in the aerospace field,[17–20] such as blowing/suction techniques,[21] actively manipulate the surrounding fluid flow by blowing or sucking air, thereby improving the surface pressure distribution on objects.[22–25] In recent years, blowing/suction techniques have been gradually applied in high-speed railway research.[26–29] Chen et al.[30] installed three circular blowing slots at the nose part of a high-speed train to investigate the drag reduction effects of blowing air at different speeds on the drag reduction effect. They found that the best drag reduction effect was achieved at 0.2 times the train velocity, resulting in an overall drag reduction of 15.43%. They also noted that the drag reduction trend becomes less significant with increasing blowing speed. Furthermore, Chen et al.[31] applied the blowing/suction technique to mitigate the lateral aerodynamic forces on trains operating under crosswind conditions, reducing the lateral forces on the head, middle, and tail cars by 18.5%, 21.7%, and 30.8%, respectively. Cui et al.[32] investigated the effects of different blowing/suction mass flow rates, positions, and quantities on the aerodynamic drag and surface pressure of the tail car of a high-speed electric multiple unit (EMU). They found that as the blowing/suction mass flow rate increased, the aerodynamic drag reduction rate of the tail car gradually increased but with diminishing returns. Additionally, when the blowing and suction mass flow rates were equal, the lower and upper edges of the port closer to the windshield experienced less pressure drag on the tail car. Moreover, with the same blowing/suction mass flow rate, increasing the number of ports resulted in better pressure drag reduction on the tail car. Shkvar et al.[33] densely distributed micro-perforations on 70% of the streamlined surface of a train car and achieved micro-blowing at 0.25% of the train's velocity, leading to a 5.25% reduction in aerodynamic drag for that specific car. They also highlighted that if all eight cars implemented micro-blowing, the train's overall aerodynamic drag could be reduced by ∼42%. Liang et al.[34] proposed the use of low-density gas jets on the train's surface to decrease aerodynamic drag significantly. They found that jetting low-density gas could effectively reduce the train's frictional drag.

In summary, the current research on blowing/suction techniques in the field of high-speed trains has shown promising results. However, the number of studies in this area is limited, making it challenging to provide sufficient data support. Furthermore, there is a lack of evaluation concerning the energy consumption and energy-saving benefits of blowing/suction techniques in existing research. Therefore, this paper adopts a numerical simulation approach to investigate the drag reduction effects and the influence on wake characteristics when employing air-blowing slots at the tail car of the TR08 maglev train at the speeds of 12 m/s (∼0.1 times the train velocity) and 24 m/s (∼0.2 times the train velocity) in the streamwise, normal to the blowing slot surface, and perpendicular blowing directions. The research findings offer new insight and data support for the development of blowing/suction drag reduction technologies in the high-speed train field and facilitate the green and sustainable development of high-speed railways.

II. RESEARCH METHOD
A. The train model

As the subject of this study, the geometric model of the TR08 maglev train is depicted in Fig. 1, where auxiliary facilities, such as headlights and door handles, have been removed to focus on its main features. The train has been scaled down to 1/16 of its original size to minimize discrepancies between numerical simulations and experiments.[35,36] After scaling, the train has a length (L) of 4.98 m, a width (W) of 0.23 m, a height (H) of 0.25 m, a distance from the top of the track to the ground of 0.078 m, and a suspension gap of 0.625 mm. At
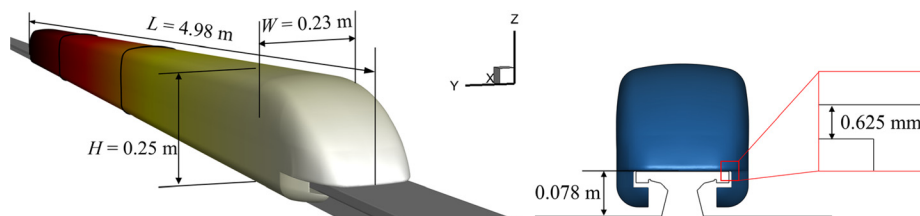

FIG. 1. Model of the TR08 maglev train.

the train speed (U) of 119.44 m/s, the corresponding average Reynolds number (Re) can be calculated as $Re = U \cdot H/v \approx 2.02 \times 10^6$, where v represents the kinematic viscosity of the fluid. Since this value exceeds the critical Reynolds number of 3.6×10^5, it is considered to enter the self-simulating region.[37,38]

B. Computational domain and boundary conditions

To simulate the infinite space in which an actual train operates using a limited computational domain, it is essential to establish an appropriate size for the domain to prevent boundary interference with the flow field around the train. As illustrated in Fig. 2, the front end of the train's nose serves as the origin of the spatial coordinate system. The boundary located $25H$ distance from the front end of the train is defined as the velocity-inlet, with a velocity vector set as (U, 0, 0). Both the ground and the track are considered as moving no-slip wall boundaries, with a velocity vector set as (U, 0, 0), to simulate the relative motion between the train and the track/ground. The boundary located $55H$ from the end of the train's tail car is designated as the pressure-outlet. The transverse width of the computational domain is set to $25H$, while the vertical height is set to $19H$. The boundaries on both sides and the top are treated as symmetry boundaries.

C. Meshing and grid independence verification

The computational domain is discretized using the hexahedral meshing method, which is comprised of the non-structured prism layer grids and structured grids in the core area. To capture turbulent information near the surface of the train, the prism layer grid is created above the train surface. This layer consists of ten layers with a thickness growth rate of 1.2 and a total thickness of ~2.18 mm. It is worth noting that the total thickness of the prism layer grid exceeds the suspension gap between the train and the track. Therefore, during the grid partitioning process, the outer layers of the mesh in that region are reduced to accommodate the suspension gap while maintaining the thickness of the first layer unchanged, as depicted in Fig. 3(b). In the current configuration of the prism layer grid, the dimensionless coefficient y^+ for the first layer thickness is ~13.28, which theoretically does not meet the requirements of improved delayed detached eddy simulation (IDDES) for y^+.[39,40] However, Fluent employs a y^+-insensitive wall treatment for all models based on the ω-equation, ensuring accurate flow structures near the wall.[41] Additionally, significant turbulent flow characteristics are observed around the train and in the wake region, which is a key focus of this study. Therefore, the grid in these regions is refined to ensure accurate computations. The refinement
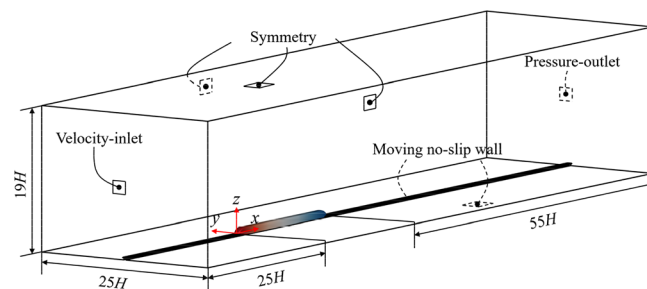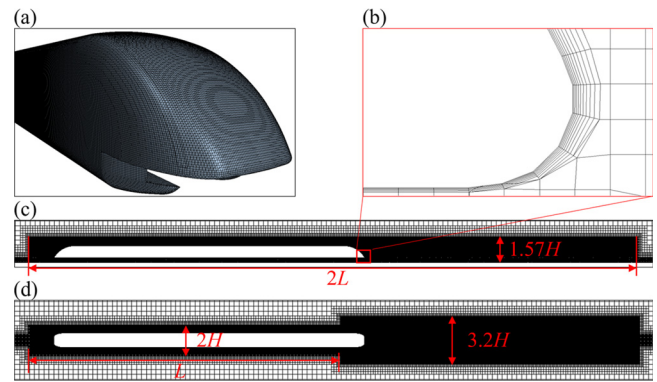

FIG. 3. Details of meshing: (a) Train surface; (b) prism layer; (c) side view of the refined zone; and (d) top view of the refined zone.

region is illustrated in Figs. 3(c) and 3(d), with grid sizes twice as those on the train surface.

Grid size is indeed crucial in computational simulations, and smaller grid sizes can capture more turbulent information and yield more accurate results, but with the cost of increased computational resources. Larger grid sizes can save computational costs but may introduce larger deviations in the obtained results. Therefore, choosing an appropriate grid size is essential to effectively utilize computational resources while ensuring the accuracy of the computed results. In this study, three different meshing schemes, namely, coarse meshing (CM), medium meshing (MM), and fine meshing (FM), were employed. The minimum grid size (Δx) of the train surface for CM, MM, and FM is set to 3.75, 2.5, and 1.25 mm, respectively. The corresponding total grid quantities are 20.5×10^6, 43.6×10^6, and 79.3×10^6.

Figure 4 provides a comparison of the aerodynamic drag coefficient [C_d, defined as Eq. (4)] and the time-averaged train-induced air flow [$\overline{U_s}$, defined as Eq. (9)] at $y = 0.55W$ and $z = 0.065H$ for the three different meshing schemes. The C_d values obtained from the head, middle, and tail cars differ among the three meshing schemes. Overall, the results from MM and FM are very close to each other, while they differ significantly from CM, especially in terms of the C_d values for the tail car. Additionally, although the overall trend of $\overline{U_s}$ of CM is similar to MM and FM, there are noticeable differences in the values, while the development trend and numerical values of $\overline{U_s}$ for MM and FM converge. Based on these observations, MM provides results that are close to FM while saving computational resources. Therefore, MM is chosen as the meshing scheme for this study.

D. Numerical solution approach and verification

In this study, the flow field information is computed using the IDDES (improved delayed detached eddy simulation) method based on the widely applied SST k–ω turbulence model.[42,43] The TR08 maglev train operates at a Mach number of ~0.35, and since the air is considered compressible, a pressure-based compressible solver was adopted.[44] The pressure-velocity coupling scheme chosen for this simulation is the semi-implicit method for pressure linked equations-consistent (SIMPLEC). The gradient in the discrete term was calculated using the least squares cell-based method. Furthermore, the pressure term was set to the second order to enhance accuracy.[45] To ensure numerical stability
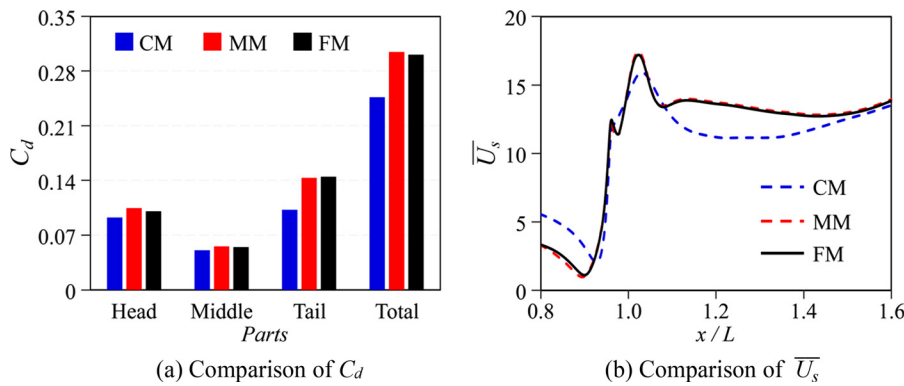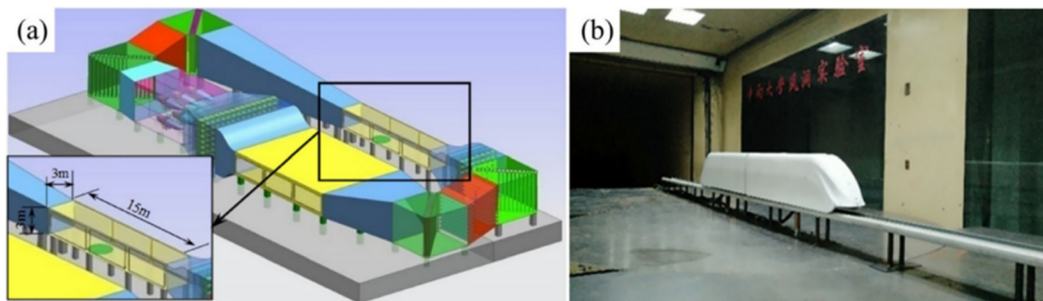

FIG. 2. Details of the computational domain.

FIG. 4. Results of the grid independence.

(a) Comparison of C_d

(b) Comparison of $\overline{U_s}$

FIG. 5. Wind tunnel test: (a) Closed-flow double-test section wind tunnel test platform and (b) train model.[46]

and accuracy, a time step size (Δt) of 2×10^{-5} was chosen, which ensures that the Courant–Friedrichs–Lewy (CFL, CFL $= U\Delta t/\Delta x$) number remains below 1.[42] In order to capture the periodic information of the turbulent flow field, the simulation was conducted for 20 000 transient steps. Afterward, a time-averaging process was performed for 10 000 steps to obtain important time-averaged physical quantities.

To validate the reliability of the numerical solution approach and the accuracy of the computed results, experimental data from a wind tunnel test conducted by Tan *et al.*[46] are referenced. The wind tunnel setup and the train model used in the experiment are shown in Fig. 5. Although the train model used in the wind tunnel test is not the same as the TR08 maglev train used in this study, both models share similar geometric characteristics. Additionally, the meshing scheme and numerical solution approach used in the validation process are consistent with the ones mentioned earlier in this study. Therefore, the validation results are considered to be highly relevant. The comparison is conducted using the dimensionless coefficient of the time-averaged surface pressure [$\overline{C_p}$, defined as Eq. (1)] at $y = 0$ on the train surface. Figure 6 presents the comparison between the numerical simulation results and the wind tunnel test results. The good agreement between the computed and experimental results demonstrates the accuracy and reliability of the chosen meshing scheme and numerical solution approach in this study.

III. RESULTS AND ANALYSIS

Due to the variation in the aerodynamic shape of the tail car, the surrounding air accelerates and separates, leading to the formation of three negative pressure regions on the tail car's surface, which is the

main reason for the generation of aerodynamic drag and lift of the tail car.[47] Additionally, the separation of air on both sides of the tail car, coupled with the downward airflow from the top, creates symmetrical vortices in the wake region, which dominate the characteristics of the train's wake flow.[48–50]

Based on this understanding, this study proposes the implementation of air-blowing slots in the streamlined section of the tail car to reduce aerodynamic drag. The air-blowing directions are arranged along the streamwise direction (X), normal to the blowing slot surface (N), and perpendicular (Z) directions, with speeds of 12 and 24 m/s. The objective is to investigate the drag reduction effect of air-blowing
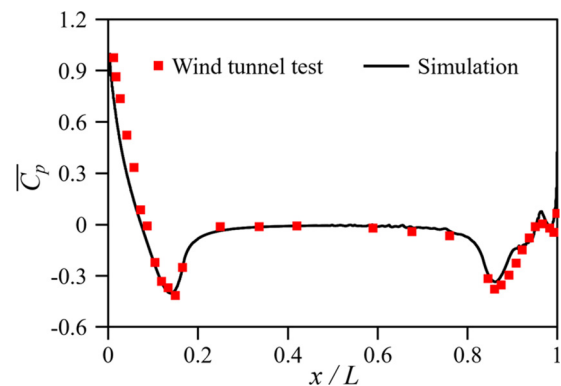

FIG. 6. Comparison of $\overline{C_p}$ at the surface ($y = 0$) of the train between wind tunnel experiment and numerical simulation.

TABLE I. Definition of all cases considered in this study.

Blowing directions	Blowing speeds	Names
. . .	. . .	Ori
X-axis		X_{12}
Normal	12 m/s	N_{12}
Z-axis		Z_{12}
X-axis		X_{24}
Normal	24 m/s	N_{24}
Z-axis		Z_{24}

and its impact on the characteristics of the wake flow. The details of all the cases can be found in Table I. For example, X_{12} stands for blowing air along the streamwise direction at the speed of 12 m/s.

The air-blowing slots are positioned starting from the transition point between the tail car's uniform cross section of the train body and the streamlined section. They are arranged longitudinally with the end point located 0.012 m above the train floor. The projected length of the slots is 0.293 m, with the projected width of 0.006 m. The total curved surface area A_b of the two slots is $\sim 0.0027 \, \text{m}^2$, as shown in Fig. 7. It is noteworthy that the formation of the symmetrical vortices in the wake region that dominates the characteristics of the train's wake flow is mainly caused by the difference in the airflow speeds around the top and the side of the tail train. This is the very reason why the air-blowing slots are set as described above.

Introducing various dimensionless coefficients is essential for a detailed analysis of the effects of different air-blowing schemes on the aerodynamic forces and wake flow characteristics of the train. The dimensionless coefficients for instantaneous pressure (C_p) are defined as follows:

$$C_p = \frac{p - p_\infty}{0.5\rho_\infty U^2}. \tag{1}$$

Here, p represents the pressure of the research object; p_∞, ρ_∞, represent the far-field freestream pressure and density, respectively. When these parameters are time-averaged, $\overline{C_p}$ denotes the time-averaged pressure coefficient.

The aerodynamic forces acting on the train are defined as follows:[51]

$$F_n = \int (p + \tau_\omega) \cdot \vec{n} dA + \int p_b \cdot \vec{n} dA_b, \tag{2}$$

$$F_{thn} = (\dot{m}_b U_b) \cdot \vec{n}. \tag{3}$$

Here, τ_ω represents the wall shear stress on the train surface. A stands for the reference area of the train. p_b and A_b represent the pressure

generated by air-blowing and the slots' area, respectively. Therefore, the term $\int p_b \cdot \vec{n} dA_b$ represents the pressure generated by air-blowing, which is defined as a part of the surface pressure (F_n) on the train. $\dot{m}_j$ and U_b are the mass flow rate and speed of air-blowing, respectively, and their product defines the thrust (F_{thn}) generated by air-blowing. $\vec{n}$ is a unit vector that determines the direction of the forces.

The dimensionless coefficients for the total aerodynamic drag (C_d), pressure drag (C_{px}), frictional drag (C_{fx}), and lift (C_l) acting on the train are defined as follows:

$$C_d = \frac{F_x + F_{thx}}{0.5\rho_\infty U^2}, \tag{4}$$

$$C_{px} = \frac{\int p \cdot \vec{x} dA + \int p_b \cdot \vec{x} dA_b}{0.5\rho_\infty U^2}, \tag{5}$$

$$C_{fx} = \frac{\int \tau_\omega \cdot \vec{x} dA}{0.5\rho_\infty U^2}, \tag{6}$$

$$C_l = \frac{F_z + F_{thz}}{0.5\rho_\infty U^2}. \tag{7}$$

The coefficient of thrust (C_{thx}) generated by air blowing is defined as follows:

$$C_{thx} = \frac{F_{thx}}{0.5\rho_\infty U^2}. \tag{8}$$

A. The influence of air-blowing on train's aerodynamic forces

Air-blowing alter the flow conditions of the surrounding air, consequently affecting the surface pressure distribution of the train.[47] Figure 8 presents the impact of different air-blowing cases on the aerodynamic drag of the tail car. It is noteworthy that the values of C_{thx} are relatively small and negative. To facilitate comparison and analysis, the corresponding values are magnified in the figure, and specific values can be found in Table II.

It can be observed that blowing air along the streamwise direction (X) yields significant drag reduction effects, with X_{12} and X_{24} reducing C_d by 2.06% and 6.53%, respectively. Conversely, blowing air along the normal (N) and perpendicular (Z) directions only increases the C_d of the tail car, and this effect is dependent on the blowing speed. The C_{fx} for different cases is very similar, consistently around 0.056. Therefore, it can be concluded that different air-blowing directions and speeds have minimal impact on the C_{fx} of the tail car, primarily influencing its C_{px}. Comparing X_{12} and X_{24}, the decrease in C_d for higher air-blowing speed is relatively similar to that of lower air-blowing speed. However,
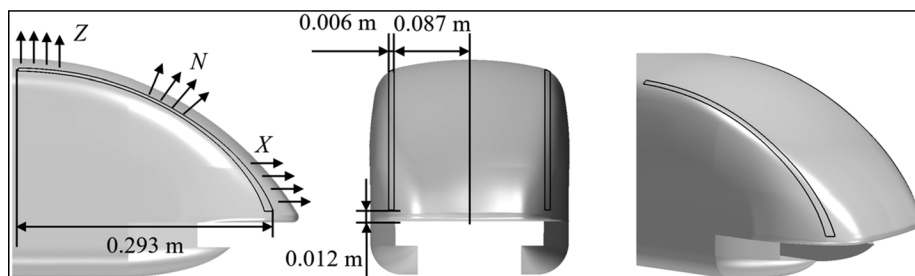
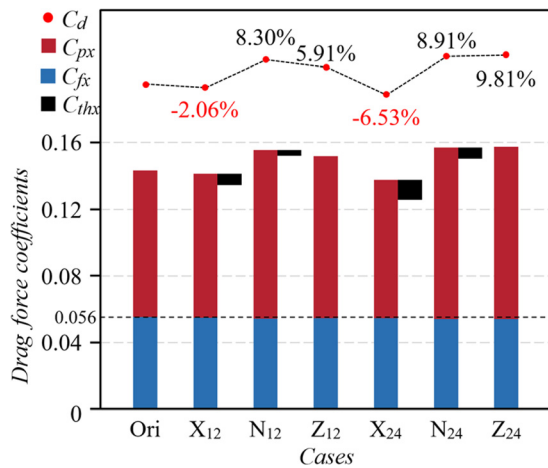**FIG. 7.** Details of the air slots and air-blowing directions.

FIG. 8. Drag reduction of the tail car in different cases.

TABLE II. Comparison of aerodynamic forces on the tail car in different cases.

Cases	Drag force				Lift force	
	C_d	C_{px}	C_{fx}	C_{thx}	C_l	Changes of C_l
Ori	0.1435	0.0877	0.0557	⋯	0.0964	⋯
X_{12}	0.1406	0.0862	0.0553	−0.0009	0.0406	−57.84%
N_{12}	0.1555	0.1009	0.0547	−0.0002	0.0193	−79.93%
Z_{12}	0.1520	0.0970	0.0551	0	0.0221	−77.09%
X_{24}	0.1342	0.0828	0.0550	−0.0036	0.0096	−90.05%
N_{24}	0.1563	0.1026	0.0546	−0.0008	0.0120	−87.51%
Z_{24}	0.1576	0.1031	0.0545	0	0.0004	−99.57%

due to the larger C_{thx} generated by higher air-blowing speed, X_{24} exhibits superior drag reduction effects. N_{12} and N_{24} have similar increase effects on C_{px}, both exceeding 8%. The effect of air-blowing speed on C_{px} is not significant. In contrast, for Z_{12} and Z_{24}, the C_{px} of the tail car is noticeably affected by the air-blowing speed. Higher air-blowing speed results in more pronounced drag increase effects, with Z_{12} and Z_{24} experiencing C_d increases of 5.91% and 9.81%, respectively.

The aerodynamic lift also affects the operational efficiency of maglev trains, but this article focuses on aerodynamic drag and does not provide an in-depth analysis of C_l. The changes in C_l of the tail cat are also presented in Table II. When blowing air at the speed of 12 m/s, X_{12} reduces the C_l by 57.84%, while both N_{12} and Z_{12} decrease C_l by nearly 80%. As the air-blowing speed increases, the reduction in C_l along the three directions intensifies. Blowing air along the perpendicular direction (Z_{24}) causes the C_l of the tail car to approach zero.

B. The influence of air-blowing on train's surface pressure

To provide a comprehensive analysis, several special positions are defined as shown in Fig. 9. Y1 represents the position where $y = 0$, while Y2 is located at a distance of 0.28 W from the train's centerline. This position is determined by the maximum negative pressure in the newly generated negative pressure zone inside the slots after blowing
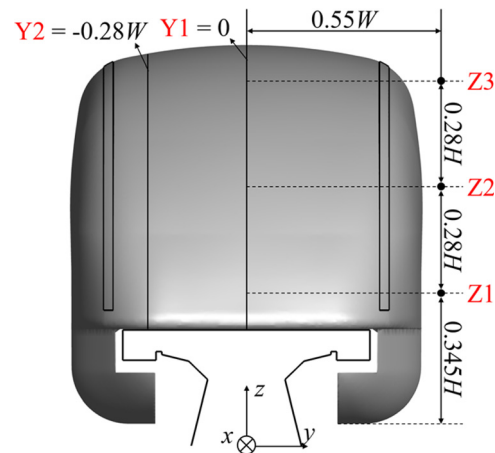

FIG. 9. Definition of some key positions.

[Fig. 10(g)]. In order to analyze the influence of air-blowing on the flow state at different heights, three heights, Z1, Z2, and Z3, are defined at a distance of 0.55 W from Y1. Among them, Z1 corresponds to the height at which the extreme negative pressure occurs at the position $x = H$ from the end of the tail car.

As mentioned earlier, there are three negative pressure zones in the streamlined section of the tail car. Based on the surface pressure distribution of the train in different cases shown in Fig. 10, it can be observed that blowing air can alleviate the negative pressure zones on the tail car's surface. This explains the significant reduction in C_l of the tail car. Among them, when blowing air at a speed of 12 m/s, the interference of N_{12} on the surrounding air around the tail car is most evident, resulting in the highest negative pressure decrease on the top and sides of the tail car. Conversely, X_{12} exhibits relatively poor alleviation effects on the three negative pressure zones, but there is a relatively large positive pressure distribution at the end of the tail car. Additionally, the surface pressure distributions of N_{12} and Z_{12} are similar. While the negative pressure zones are alleviated, a small range of negative pressure is generated on the inside of the air-blowing slots, leading to increased aerodynamic drag of the tail car. These phenomena become more pronounced when blowing air at the speed of 24 m/s.

The flow direction and normal component of surface pressure on the train determine the magnitude of aerodynamic drag and lift. In the streamlined surface section of the tail car, the closer the pressure is to the end, the greater the flow direction component, and thus, the more significant its contribution to aerodynamic drag. Figure 11 presents the surface pressure distribution curves at Y1 and Y2. The black dashed lines in the figure represent the position of the beginning of the air slots (BOS) and the middle position of the streamlined surface (MOS), which divides the streamlined tail car into two parts: one part with smaller flow direction component (P1) and another part with larger flow direction component (P2). Observing the pressure variations at the Y1 position in Figs. 11(a) and 11(b), it can be observed that the negative pressure decrease on the tail car surface largely occurs in P1, resulting in a significant reduction in C_l. Within the P2 range, the negative pressure on the tail car surface increases, with N_{12} and Z_{12} showing greater increases compared to X_{12}. When blowing air at the speed of 24 m/s, the increase in negative pressure within the P2 range is reduced for X_{24}, while N_{24}
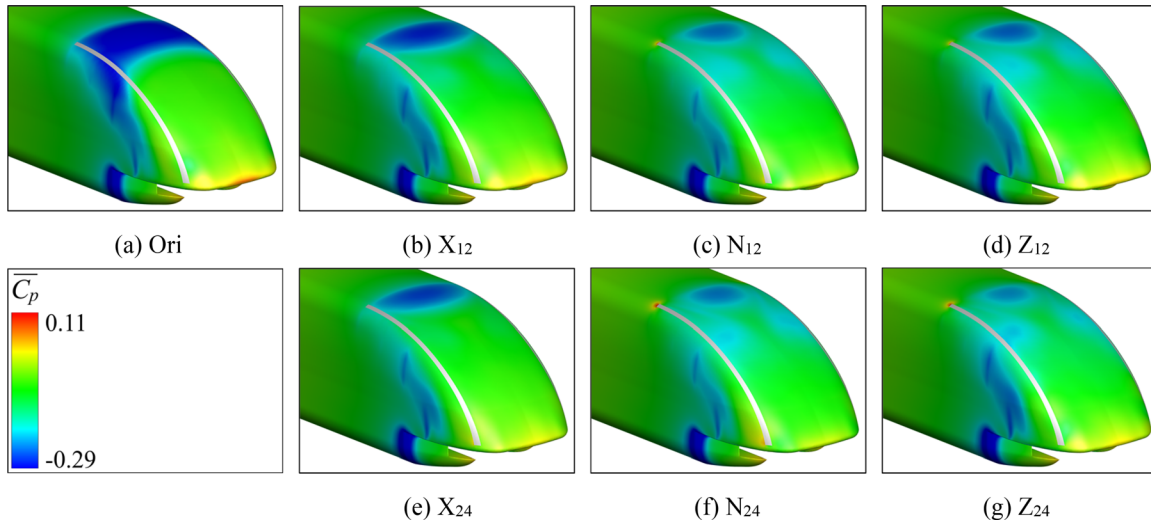
FIG. 10. Surface mean-pressure distributions of the tail cars in different cases.
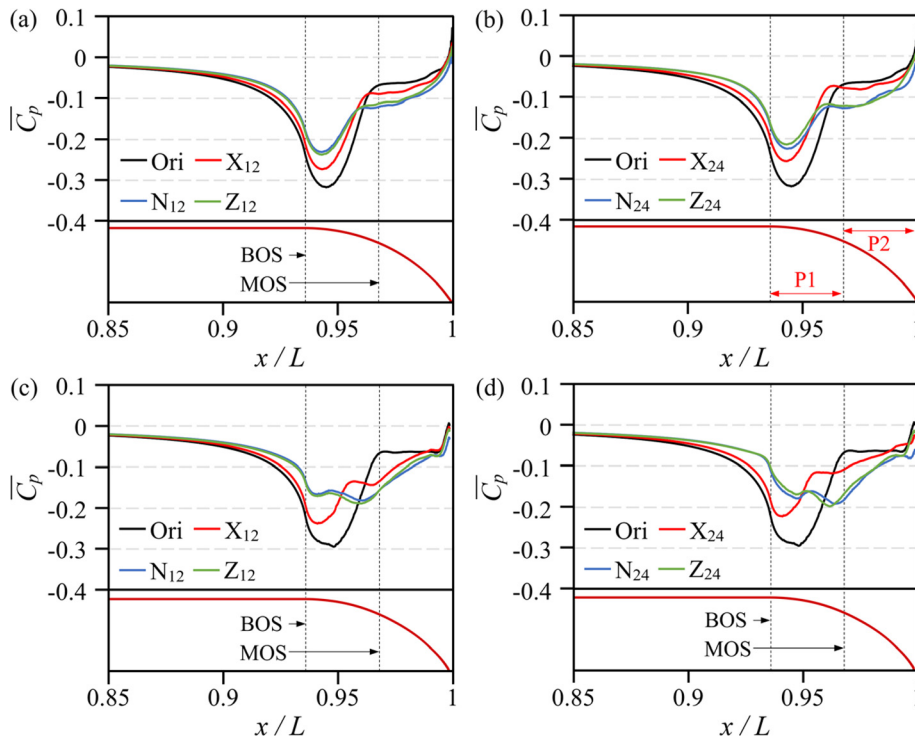
FIG. 11. Longitudinal surface mean-pressure curves: (a) Y1, 12 m/s; (b) Y1, 24 m/s; (c) Y2, 12 m/s; and (d) Y2, 24 m/s.

and Z_{24} exhibit further increases in negative pressure. Similarly, for the Y2 position in Figs. 11(c) and 11(d), although the negative pressure decrease within the P1 range is more pronounced for N_{12}, Z_{12}, N_{24}, and Z_{24}, the increase in negative pressure within the P2 range is even more significant. These observations explain why blowing air along the streamwise direction reduces drag while blowing air in the normal and perpendicular directions increases it.

C. The influence of air-blowing on wake flow and train-induced air flow

The time-averaged pressure distribution ($\overline{C_p}$) in different positions of the wake region of a maglev train is shown in Fig. 12. In the figure, the regions with larger negative pressure correspond to the locations of vortices. Z1 is defined as the height at which the maximum negative pressure occurs, measured from the position $x = H$ away

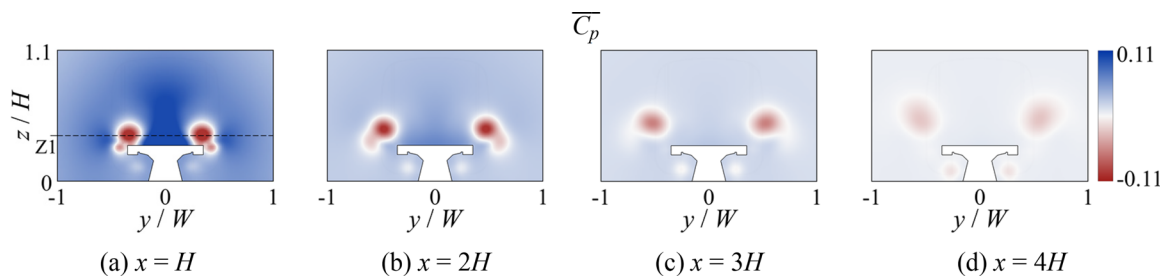**FIG. 12.** Mean pressure distribution on the z–y plane at different streamwise locations.

from the end of the tail car. It can be observed that the wake vortex gradually dissipates along the flow direction, with its scale increasing and moving upward and sideways along the span direction.

Figure 13(a) shows the variation of instantaneous pressure (C_p) at position Z1, located at a distance $x = H$ from the end of the tail car, for the last 2500 computational steps (S_{tep}). Within this spatial region, the C_p distribution along the span direction exhibits relatively stable characteristics. The regions with larger negative pressure correspond to the locations of vortices, with higher positive pressure between the vortices and lower pressure on the sides. This pattern also reflects the distribution of fluid flow velocity in the space. The position marked as P

represents the center of the maximum negative pressure in Fig. 12(a). It is worth noting that due to the high turbulence characteristics near the wake region, the position of the vortex center is not stable but oscillates within a certain spatial range. The frequency of oscillation can be considered as the shedding frequency (St) of the vortices. The power spectral density (PSD) of St is obtained based on the instantaneous pressure data at point P, as shown in Fig. 13(b). $St \approx 0.3$ stands out as the characteristic shedding frequency of the wake vortices.

Figure 14 illustrates the variation of C_p at position Z1, located at a distance $x = H$ from the end of the tail car, for the last 2500 computational steps (S_{tep}) in different cases. By comparing the cases, it can be
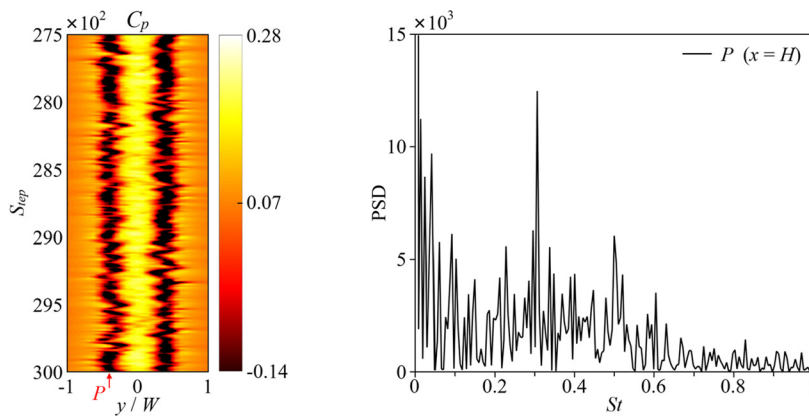
(a) Fluctuation of instantaneous pressure C_p over calculation step S_{tep} at Z1 ($x = H$)

(b) Power spectral density of St at point P

FIG. 13. Characteristics of wake turbulence.
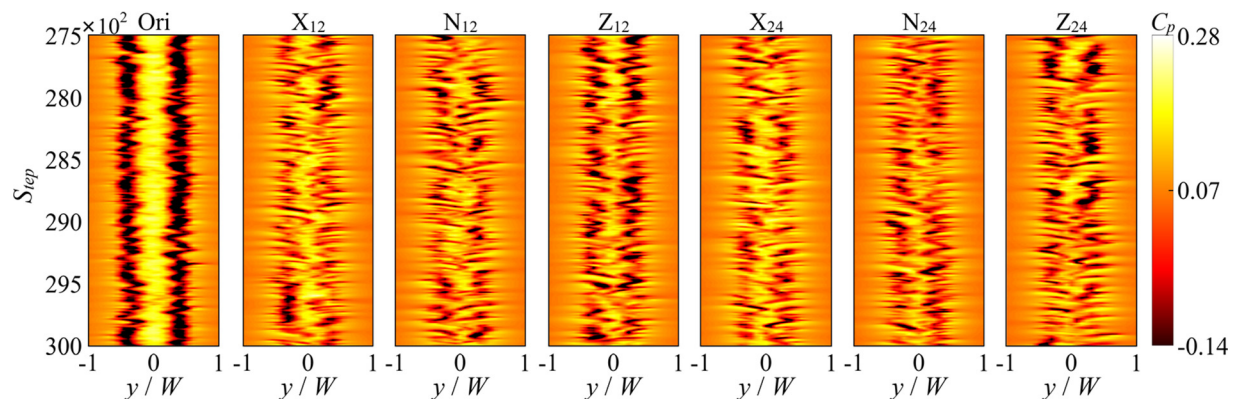
FIG. 14. Fluctuation of instantaneous pressure C_p over calculation step at Z1 ($x = H$) in different cases.

observed that after air-blowing, the pressure distribution of X_{12}–Z_{24} at this spatial position remains symmetric along the centerline, exhibiting fluctuating negative pressure with a spanwise location closer to the center of the train compared to the Ori. However, the negative pressure fluctuations of X_{12}–Z_{24} are not as pronounced as in the Ori case. As time progresses, the pressure distribution of X_{12}–Z_{24} at this spatial position exhibits strong turbulent characteristics.

The pressure distribution and intensity at position X_{12}–Z_{24} in Fig. 14 also reflect the fluid flow conditions at that spatial location. Figure 15 presents the time-averaged fluid velocity distributions in the x–y plane at positions Z1–Z3 for all different cases. In Fig. 15(a), the wake of the Ori exhibits a distinct crescent shape, which is a typical characteristic of a wake vortex structure. The vortices spread along the span direction, leading to an increase in the wake width (W_w) in the

FIG. 15. Velocity magnitude distribution on the x–y plane at different altitudes (Z1–Z3) in different cases.

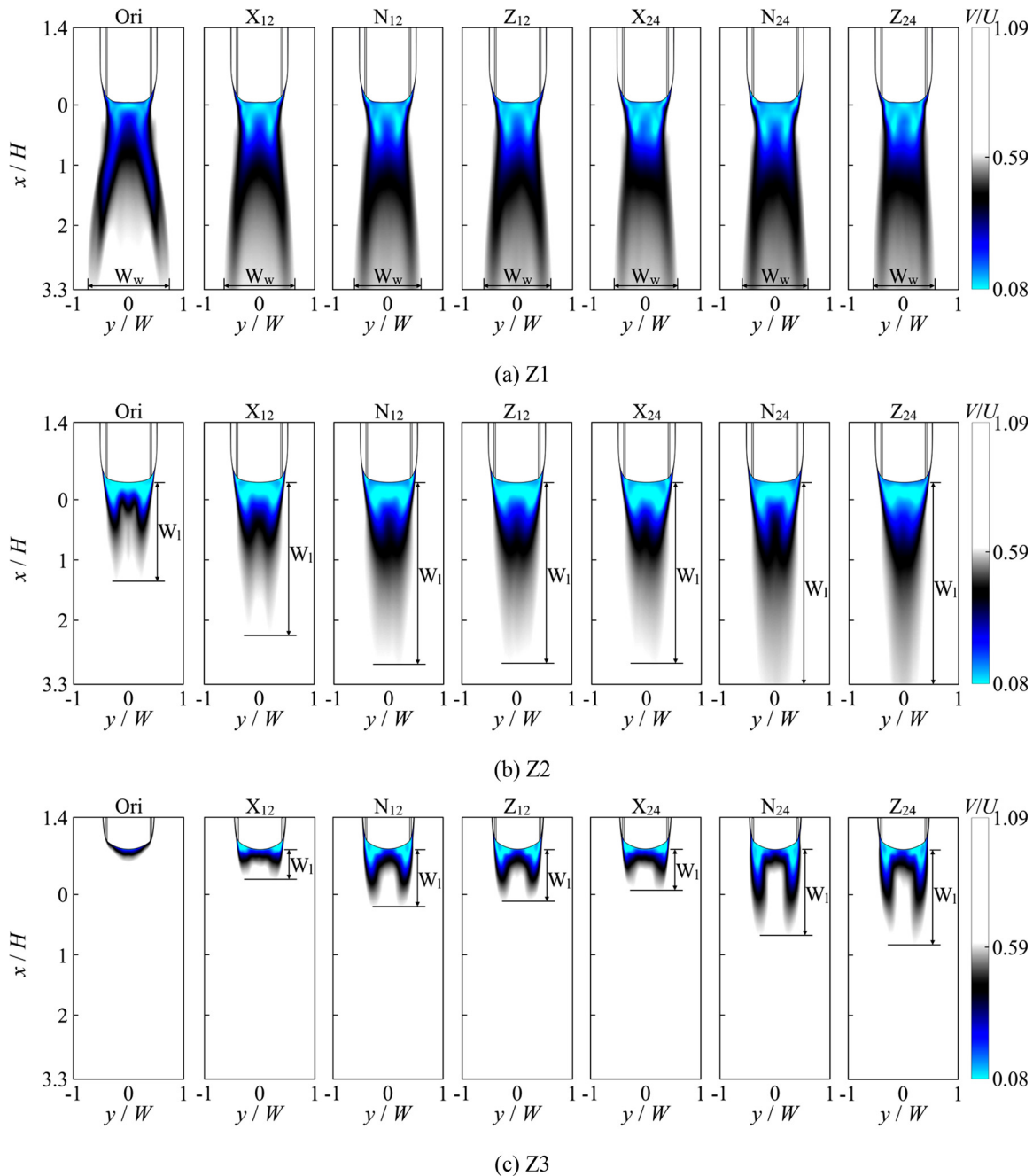streamwise direction. As the vortices evolve and dissipate along the streamwise direction, their vorticity gradually weakens, and the streamwise motion characteristics become more prominent, as indicated by an increasing velocity in the crescent-shaped wake. After air-blowing, the flow velocity near the surface of the train does not show significant differences, but that in the near-wake region significantly decreases. Furthermore, the crescent-shaped wake feature remains after air-blowing, but its formation location is delayed, and the flow velocity significantly increases. This indicates that the shedding of vortices is postponed after air-blowing, and the vortices exhibit lower vorticity, resulting in a more pronounced streamwise flow characteristic and a reduced W_w. There are noticeable differences in the wake characteristics between X_{12} and X_{24}, as well as Z_{12} and Z_{24}, where the low-speed portion of the crescent-shaped wake and W_w further decrease. However, the differences between N_{12} and N_{24} are not significant.

The wake length (W_l) at position Z2 for the Ori case is smaller, whereas after air-blowing, the W_l increases for different cases. This indicates that air-blowing is effective in impeding the acceleration of the surrounding air near the tail car. Among them, the W_l for N_{12} and Z_{12} is similar and greater than that for X_{12}, suggesting that blowing air along the streamwise direction has a relatively smaller inhibitory effect on the acceleration of the air around the tail car. This is consistent with the pressure distribution characteristics shown in Fig. 10. The aforementioned phenomenon increases with the increase in the air-blowing speed.

At position Z3, the wake length (W_l) for the Ori case further decreases, and to a lesser extent, X_{12} and X_{24} interfere with the fluid flow at that height. When blowing air at the speed of 12 m/s, the disturbance caused by N_{12} is the greatest. However, when blowing air at the speed of 24 m/s, the degree of change in the airflow state is the greatest in the case of Z_{24}.

The vorticity can visually express the intensity and direction of vortices. Figures 16(a) and 16(b) depict the time-averaged streamwise vorticity $\overline{\omega_x}$ at distances $x = H$ and $x = 2H$ from the end of the tail car for all different cases. The vortices in the wake of the maglev train are primarily composed of two pairs of counter-rotating vortices above and below the track surface. However, due to the geometric irregularity of the track, another pair of counter-rotating vortices forms on either side. By observing the $\overline{\omega_x}$ at two different streamwise locations for the Ori case, it can be seen that the vortices on the track surface and the sides develop along the spanwise direction, with their vorticity gradually decreasing. The $\overline{\omega_x}$ for X_{12}–Z_{12} indicates that blowing air alters the intensity and position of the vortices. The $\overline{\omega_x}$ of the vortices on the track surface at $x = H$ from the end of the tail car significantly decreases and is closer to the train's centerline. Additionally, the change in vortices is similar for N_{12} and Z_{12}, but relatively higher compared to X_{12}. When blowing air at the speed of 24 m/s, the $\overline{\omega_x}$ for X_{24} and N_{24} further decreases, with X_{24} exhibiting the greatest change in the wake vortices. Conversely, the $\overline{\omega_x}$ for Z_{24} decreases compared to Z_{12}, particularly at $x = 2H$ from the end of the tail car, but the decrease is relatively small. To sum up, it can be concluded that blowing air causes the vortices on the track surface to be closer to the train's centerline with a smaller $\overline{\omega_x}$. Combining this analysis with the previous discussion, this phenomenon occurs due to the air-blowing hindering air acceleration and delaying vortex shedding, resulting in weaker turbulence intensity in the near-wake region and slower vortex

development at the same spatial location. Furthermore, the influence of air-blowing speed on the wake vortices is more pronounced when blowing air along the streamwise direction, whereas the wake vortices are less sensitive to the variation in blowing speed when blowing air perpendicularly.

In general, vortices at the same spatial location follow the principle that larger vorticity corresponds to larger vortex scales. Figures 16(c) and 16(d) represent the vector distributions of the spanwise-averaged air velocity $\overline{v}$ and the vertical-averaged air velocity $\overline{w}$, respectively. Clearly, the vortex scales decrease after air-blowing. At $x = H$ from the end of the tail car, where the air is blown at the speed of 12 m/s, both N_{12} and Z_{12} exhibit a significant reduction in vortex scale, and their reductions are relatively close to each other. However, X_{12} shows a relatively smaller decrease in the vortex scale. At $x = 2H$ from the end of the tail car, there are no significant differences in vortex scale among N_{12}, Z_{12}, and X_{12}. At $x = H$ from the end of the tail car for X_{24}–Z_{24}, the vortex scale further decreases but not significantly. However, at $x = 2H$ from the end of the tail car, there is a notable reduction in the vortex scale.

As mentioned earlier, blowing air affects the acceleration of the surrounding air around the tail car, thereby altering the wake flow structure of the maglev train. The train-induced air flow (U_s) in wake aera poses a safety hazard to passengers on platforms, trackside workers, and track infrastructure.[52] This section analyzes the impact of different air-blowing cases on the wake flow from the perspective of U_s, which is defined as follows:

$$U_s = \sqrt{(U-u)^2 + v^2}. \qquad (9)$$

Figure 17 represents the development curve of the U_s along the streamwise direction at the position 0.55 W away from the train's central line for varying heights of Z1–Z3 (see Fig. 9). Table III provides the positive peak values and corresponding percentage reductions of the U_s in the wake region at different heights for different cases. In general, as the height increases, the time-averaged maximum velocity $\overline{U_{smax}}$ gradually decreases, and the location of which moves closer to the tail car. Blowing air has a significant effect in reducing $\overline{U_{smax}}$ and delaying the occurrence of the peak.

At the Z1 height, after blowing air at the speed of 12 m/s, the $\overline{U_{smax}}$ of X_{12}–Z_{12} decreases compared to the Ori. Among them, N_{12} shows the largest decrease in $\overline{U_{smax}}$, ~55%, while X_{12} exhibits the smallest reduction, around 45%. When blowing air at the speed of 24 m/s, the reduction in $\overline{U_{smax}}$ ($\Delta \overline{U_s}$) for X_{24} and Z_{24} further increases. However, when blowing air in the normal direction (N_{24}), the $\Delta \overline{U_s}$ is weaker than that of N_{12}. The maximum of $\Delta \overline{U_s}$ occurs when blowing air perpendicularly at the speed of 24 m/s (Z_{24}), where $\Delta \overline{U_s}$ is ~61.91%. Additionally, blowing air has a noticeable impact on the location of the $\overline{U_{smax}}$ at this height. In the case of Ori, the $\overline{U_{smax}}$ appears near $2H$ from the end of the tail car. After air-blowing, the location of the $\overline{U_{smax}}$ is shifted ~$1H$ rearward for all cases. Notably, when blowing air in the streamwise direction, the location of $\overline{U_{smax}}$ is significantly influenced by the air-blowing speed.

At the Z2 height, different air-blowing strategies result in relatively low and similar levels of reduction in the $\overline{U_{smax}}$. After blowing air at the speed of 12 m/s, X_{12}–Z_{12} exhibit a reduction of ~14% in $\overline{U_{smax}}$. When blowing air at the speed of 24 m/s, the $\Delta \overline{U_s}$ increases for
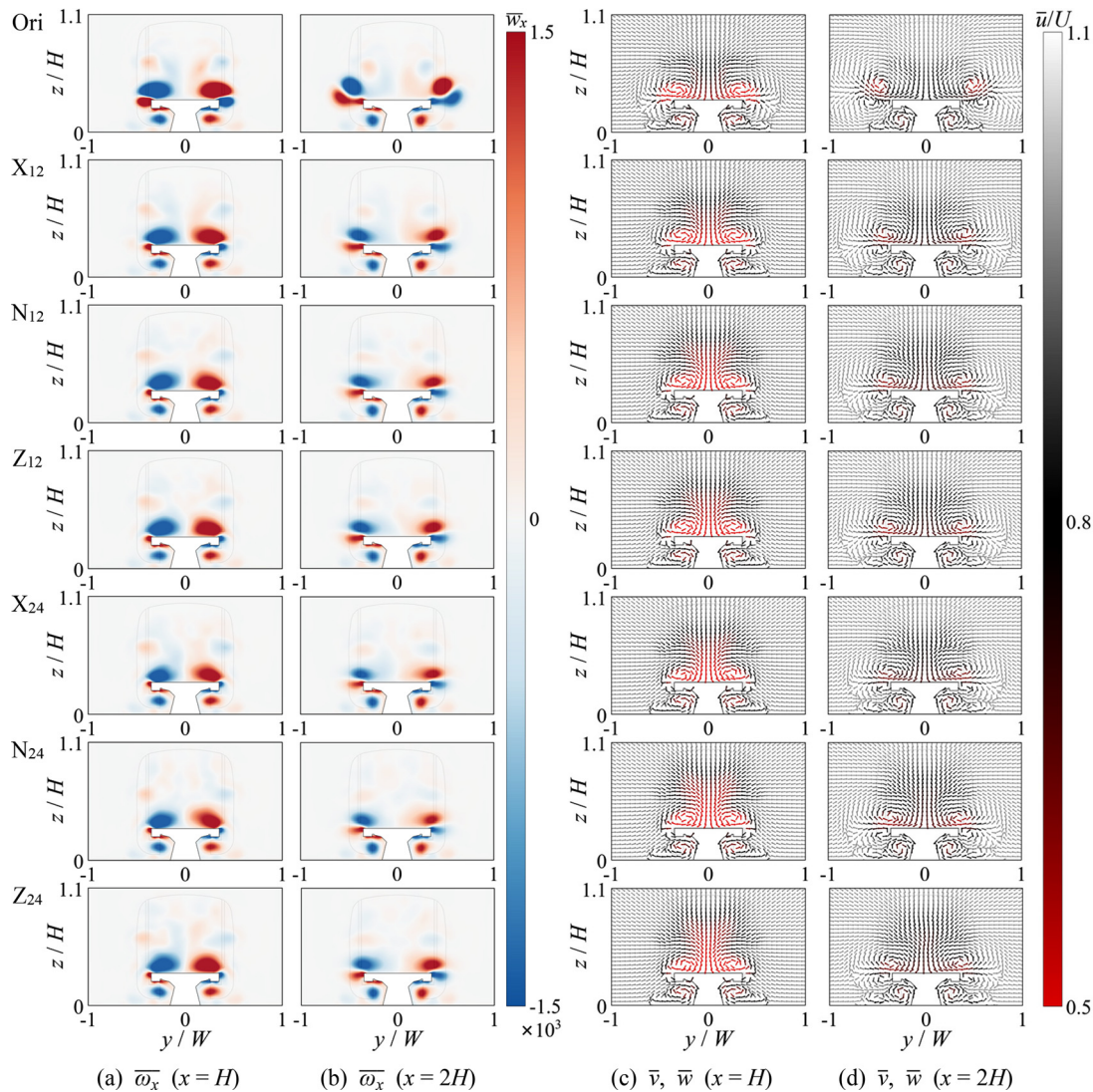
FIG. 16. Characteristics of wake flow.

X_{24} and Z_{24}, while that for Z_{24} is decreased In general, the $\overline{U_{smax}}$ for X_{12}–Z_{24} ranges from 17 to 18 m/s at this height. This indicates that blowing air at this height can reduce the $\overline{U_{smax}}$, but the $\Delta \overline{U_s}$ is not strongly correlated with the air-blowing direction and speed. The maximum of $\Delta \overline{U_s}$ occurs when blowing air in the normal direction at the speed of 24 m/s (N_{24}), with the value of 17.98%. Furthermore, the impact of air-blowing on the location of the $\overline{U_{smax}}$ at this height is relatively weak. Both before and after air-blowing, the location of the $\overline{U_{smax}}$ remains within a range of $1H$ from the end of the tail car.

At the Z3 height, after blowing air at the speed of 12 m/s, X_{12} and Z_{12} exhibit similar levels of $\Delta \overline{U_s}$, while N_{12} shows the highest reduction at 32.99%. When blowing air at the speed of 24 m/s, X_{24}-Z_{24} experience an increase in $\Delta \overline{U_s}$, with the maximum of $\Delta \overline{U_s}$ occurring when blowing air in the normal direction at the speed of 24 m/s (N_{24}) with the value of 38.27%. Furthermore, the impact of air-blowing on the

location of the $\overline{U_{smax}}$ at this height is also relatively weak. Both before and after air-blowing, the location of the $\overline{U_{smax}}$ remains within the region of the streamlined part of the tail car.

D. Energy efficiency analysis

Based on the previous discussion, it is evident that blowing air along the streamwise direction can achieve significant drag reduction effects. X_{12} and X_{24} result in a reduction in C_d by ∼2.06% and 6.53%, respectively. However, the energy consumption caused by air-blowing is also a part that needs to be considered. In this section, the aim is to determine the relationship between air-blowing speed and drag reduction efficiency and evaluate the energy-saving efficiency of X_{12} and X_{24} from the energy perspective. The energy saved due to drag reduction by air-blowing is defined as E_s, where ΔF_d in Eq. (10) represents the
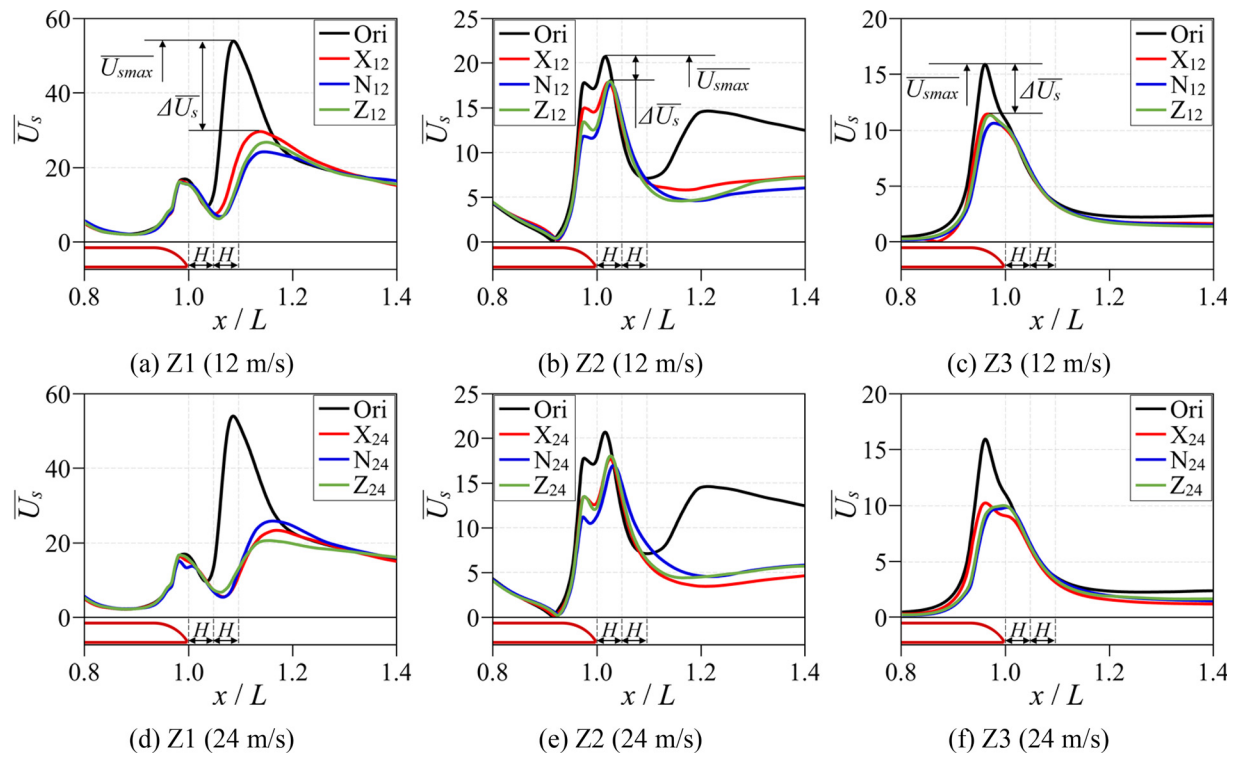
FIG. 17. Comparison of train-induced air flow at different altitudes (Z1–Z3) in different cases.

decrease in aerodynamic drag force due to air-blowing and U is the reference velocity, which in this case is defined as the train's operating speed. It is worth mentioning that E_s does not represent the actual energy saved, as it needs to be compared with the energy consumption caused by air-blowing. Therefore, ΔF_d is converted into an energy form. Equation (11) defines the dimensionless coefficient C_{Es} for E_s,

$$E_s = \Delta F_d U, \tag{10}$$

$$C_{Es} = \frac{E_s}{0.5\rho U^3 A}, \tag{11}$$

TABLE III. The positive peak value $\overline{U_{smax}}$ and the difference $\Delta\overline{U_s}$ of train-induced air flow at different altitudes (Z1–Z3) in different cases.

	Z1		Z2		Z3	
Cases	$\overline{U_{smax}}$ (m/s)	$\Delta\overline{U_s}$	$\overline{U_{smax}}$ (m/s)	$\Delta\overline{U_s}$	$\overline{U_{smax}}$ (m/s)	$\Delta\overline{U_s}$
Ori	54.10	⋯	20.80	⋯	15.96	⋯
X_{12}	29.78	−44.96%	17.92	−13.86%	11.52	−27.78%
N_{12}	24.31	−55.06%	17.76	−14.63%	10.69	−32.99%
Z_{12}	26.89	−50.30%	18.04	−13.28%	11.40	−28.56%
X_{24}	23.37	−56.81%	17.78	−14.53%	10.25	−35.76%
N_{24}	25.88	−52.17%	17.06	−17.98%	9.85	−38.27%
Z_{24}	20.61	−61.91%	18.13	−12.86%	10.01	−37.25%

$$C_{Eb} = \frac{W_b}{0.5\rho U^3 A} = \frac{n\left(0.5\rho_b U_b^2 A_b\right) U_b}{0.5\rho U^3 A}. \tag{12}$$

C_{Eb} represents the input energy coefficient of the air-blowing, and its definition is given in Eq. (12).[53,54] In this study, the air-blowing slots are arranged on the surface of the train, and the boundary condition is defined as the velocity-inlet. There is no pressure loss caused by the presence of pipes in the actual scenario, thus satisfying the prerequisite condition of this equation.[51] In Eq. (12), W_b can be regarded as the energy consumed by air-blowing, n represents the number of blowing slots, ρ_b and U_b are the density and speed of the blowing air, respectively, and A_b is the total area of the two air-blowing slots. Furthermore, the net energy saving ΔC_E is defined as the difference between C_{Es} and C_{Eb}, and the results are presented in Table IV.

From the data in Table IV, it can be observed that ΔC_E for X_{12} is ∼58.69% of C_{Es}, indicating a significant energy-saving benefit. However, for X_{24} with higher air-blowing speed, ΔC_E is negative, indicating that the energy consumption caused by air-blowing exceeds the energy saved due to drag reduction. However, with ΔC_E close to 0, it

TABLE IV. Energy comparison between X_{12} and X_{24}.

Cases	U_b (m/s)	C_{Es}	C_{Eb}	ΔC_E
X_{12}	12	0.0029	0.0012	0.0017
X_{24}	24	0.0093	0.0096	−0.0003

can be considered that energy consumption and energy saving are balanced. Therefore, although higher air-blowing speed can achieve greater drag reduction effects, the energy consumption associated with air-blowing needs to be taken into consideration. It is important to emphasize that the energy-saving results in this subsection do not reflect the actual outcomes. The conclusions are intended as theoretical references for future practical application of this method in engineering projects.

IV. CONCLUSIONS

This study focuses on the aerodynamic drag issue of high-speed maglev trains. Numerical simulation is employed to investigate the drag reduction effects and the influence on wake characteristics when air-blowing slots are arranged on the tail car, and blowing air along the streamwise direction (X), normal to the blowing slot surface (N), and perpendicular direction (Z), at the speeds of 12 m/s (X_{12}, N_{12}, Z_{12}) and 24 m/s (X_{24}, N_{24}, Z_{24}). By analyzing the aerodynamic drag, aerodynamic lift, and airflow characteristics in the wake region of the train, the following conclusions are drawn:

(1) Blowing air along the streamwise direction (X) consistently achieves significant drag reduction effects, with reductions of 2.06% and 6.53% for X_{12} and X_{24}, respectively. In contrast, blowing air along the normal (N) and perpendicular direction (Z) only increases the aerodynamic drag. Moreover, all different air-blowing cases reduces the lift force acting on the tail car. In particular, Z_{24} results in nearly zero aerodynamic lift of the tail car.

(2) The wake of the TR08 maglev train exhibits a distinct crescent-shaped pattern, which is a typical characteristic of the presence of wake vortices. Blowing air causes a significant decrease in the airflow velocity near the wake region. The vortices on the track surface are displaced toward the centerline of the train, the vorticity of the vortices is reduced, and the vortex shedding is delayed. In the cases of X, the influence of the air-blowing speed on the wake vortices is more pronounced. Conversely, for the cases of Z, the wake vortices are less sensitive to changes in the air-blowing speed.

(3) Blowing air significantly reduces the peak value of the train-induced air flow ($\overline{U_{smax}}$). At the height of Z1, after blowing air at the speed of 12 m/s, the N_{12} exhibits the highest relative reduction in $\overline{U_{smax}}$, ~55%, while the X_{12} configuration shows the smallest reduction, ~45%. After blowing air at the speed of 24 m/s, the Z_{24} reduces $\overline{U_{smax}}$ by 61.91%. Additionally, at this height, blowing air causes a delayed occurrence of the $\overline{U_{smax}}$, with the location being more influenced by the air-blowing speed when blowing air along the streamwise direction.

(4) The cases of X_{12} provide considerable energy-saving benefits. However, the energy consumption associated with blowing air at higher speed in the cases of X_{24} exceeds the energy saved from its drag reduction. This indicates that although higher air-blowing speed can achieve greater drag reduction effects, the energy consumption caused by air-blowing needs to be taken into consideration.

The method of implementing the air-blowing slots at the train tail exhibits significant drag reduction effects. The extension and investigation of active control methods on high-speed maglev trains provide new approaches for drag reduction, as well as contribute to further increasing the operating speed of high-speed maglev trains. Moreover, some of the air-blowing schemes obtained from this study, which demonstrate an increase in drag, can also be applied in scenarios involving emergency braking of trains. In conclusion, the air-blowing active control technique holds substantial research value and significance in the field of high-speed trains.

AUTHOR DECLARATIONS
Conflict of Interest

The authors have no conflicts to disclose.

Author Contributions

Zheng-Xin Che: Software (equal); Writing – original draft (equal). **Zheng-Wei Chen:** Supervision (equal); Writing – review & editing (equal). **Yi-Qing Ni:** Investigation (equal); Supervision (equal). **Sha Huang:** Data curation (equal); Writing – review & editing (equal). **Zhi-Wei Li:** Validation (equal); Writing – review & editing (equal).

DATA AVAILABILITY

The data that support the findings of this study are available from the corresponding author upon reasonable request.

REFERENCES

[1] S. Huang, Z. Li, and M. Yang, "Aerodynamics of high-speed maglev trains passing each other in open air," J. Wind Eng. Ind. Aerodyn. **188**, 151 (2019).

[2] S.-S. Ding, J.-L. Liu, and D.-W. Chen, "Aerodynamic design of the 600 km/h high-speed maglev transportation system," J. Exp. Fluid Mech. **37**, 1 (2023).

[3] M. Yang, J. Du, Z. Li, S. Huang, and D. Zhou, "Moving model test of high-speed train aerodynamic drag based on stagnation pressure measurements," PLoS ONE **12**, e0169471 (2017).

[4] X. H. Zhang, Y. Jiang, and T. Li, "Effect of streamlined nose length on the aerodynamic performance of a 800 km/h evacuated tube train," Fluid Dyn. Mater. Process. **16**, 67 (2020).

[5] Z. X. Sun, Y. F. Yao, D. L. Guo, G. W. Yang, S. B. Yao, Y. Zhang, D. W. Chen, G. B. Li, K. M. Shang, and L. Jia, "Research progress in aerodynamic optimization of high-speed trains," Chin. J. Theor. Appl. Mech. **53**, 51 (2021).

[6] J. Muñoz-Paniagua and J. García, "Aerodynamic surrogate-based optimization of the nose shape of a high-speed train for crosswind and passing-by scenarios," J. Wind Eng. Ind. Aerodyn. **184**, 139 (2019).

[7] J. Munoz-Paniagua and J. García, "Aerodynamic drag optimization of a high-speed train," J. Wind Eng. Ind. Aerodyn. **204**, 104215 (2020).

[8] Z. Wu, Z. Xie, P. Wang, and W. Ding, "Aerodynamic drag performance analysis of different types of high-speed train pantograph fairing," J. Appl. Sci. Eng. **23**, 509 (2020).

[9] W. Liu, Z. Ji, D. Guo, G. Yang, G. Zhou, and K. Ren, "Effects of bottom deflectors on aerodynamic drag reduction of a high-speed train," Acta Mech. Sin. **38**, 321251 (2022).

[10] T. Li, H. Liang, J. Zhang, and J. Zhang, "Numerical study on aerodynamic resistance reduction of high-speed train using vortex generator," Eng. Appl. Comput. Fluid Mech. **17**, e2153925 (2023).

[11] H. Du, D. Zhou, S. Meng, and C. Luo, "Effect of vortex generators on the aerodynamic performance of high-speed trains," Flow. Turbul. Combust. **109**, 627 (2022).

[12] J. Zhang, F. Huang, Y. Yu, S. Han, Y. Ding, and G. Gao, "A novel wake flow control method for drag reduction of a high-speed train with vortex generators installing on streamlined tail nose," Phys. Fluids **35**, 105139 (2023).

[13] Z. Zhu, J. Li, H. Peng, and D. Liu, "Nature-inspired structures applied in heat transfer enhancement and drag reduction," Micromachines **12**, 656 (2021).

[14] D. Zhou, L. Wu, C. Tan, and T. E. Hu, "Study on the effect of dimple position on drag reduction of high-speed maglev train," Transp. Safety Environ. **3**, tdab027 (2021).

[15] D. Wang, C. Chen, and C. Deng, "The use of non-smooth surfaces to control the wake of a high speed train," Proc. Inst. Mech. Eng., Part F **234**, 1041 (2020).

[16] D. Chen, Y. Liu, H. Chen, and D. Zhang, "Bio-inspired drag reduction surface from sharkskin," Biosurf. Biotribol. **4**, 39 (2018).

[17] D. J. Zhao, Y. K. Wang, W. W. Cao, and P. Zhou, "Optimization of suction control on an airfoil using multi-island genetic algorithm," Procedia Eng. **99**, 696 (2015).

[18] R. Wahidi and D. H. Bridges, "Effects of distributed suction on an airfoil at low Reynolds number," AIAA J. **50**, 523 (2012).

[19] S. F. Tardu and O. Doche, "Active control of the turbulent drag by a localized periodical blowing dissymmetric in time," Exp. Fluids **47**, 19 (2009).

[20] M. Quadrio, A. Chiarini, J. Banchetti, D. Gatti, A. Memmolo, and S. Pirozzoli, "Drag reduction on a transonic airfoil," J. Fluid Mech. **942**, R2 (2022).

[21] Z. Li, X. Liu, P. Lv, and Y. Feng, "Drag reduction of blowing-based active control in a turbulent boundary layer," Phys. Fluids **34**, 115146 (2022).

[22] L. Zhang, X. Shan, and T. Xie, "Active control for wall drag reduction: Methods, mechanisms and performance," IEEE Access **8**, 7039 (2020).

[23] X. Chen, S. Zhong, O. Ozer, and A. Weightman, "Control of afterbody vortices from a slanted-base cylinder using sweeping jets," Phys. Fluids **34**, 075115 (2022).

[24] R. Jackson, Z. Wang, and I. Gursul, "Control of upswept afterbody vortices using continuous and pulsed blowing," J. Aircr. **57**, 76 (2020).

[25] R. Ma, Z.-H. Gao, L.-S. Lu, and S.-S. Chen, "Skin-friction drag reduction by local porous uniform blowing in spatially developing compressible turbulent boundary layers," Phys. Fluids **34**, 125130 (2022).

[26] S. Huang, Y. Yu, Z. Li, and Z. Che, "Study of aerodynamic drag reduction of high-speed train based on tail jet-flow control," J. China Railway Soc. **43**, 38 (2021).

[27] N. Gao and J. Du, "Research on drag reduction flow control technology for high-speed EMUs," J. Phys.: Conf. Ser. **2455**, 012003 (2023).

[28] X. Chen, S. Zhong, O. Ozer, and A. Weightman, "Drag reduction of a slanted-base cylinder using sweeping jets," Phys. Fluids **34**, 105101 (2022).

[29] Z.-W. Chen, Z.-H. Guo, Y.-Q. Ni, T.-H. Liu, and J. Zhang, "A suction method to mitigate pressure waves induced by high-speed maglev trains passing through tunnels," Sustainable Cities Soc. **96**, 104682 (2023).

[30] Z.-W. Chen, G.-Z. Zeng, Y.-Q. Ni, T.-H. Liu, J.-Q. Niu, and H.-D. Yao, "Reducing the aerodynamic drag of high-speed trains by air blowing from the nose part: Effect of blowing speed," J. Wind Eng. Ind. Aerodyn. **238**, 105429 (2023).

[31] Z.-W. Chen, Y.-Q. Ni, Y.-W. Wang, S.-M. Wang, and T.-H. Liu, "Mitigating crosswind effect on high-speed trains by active blowing method: A comparative study," Eng. Appl. Comput. Fluid Mech. **16**, 1064 (2022).

[32] H. Cui, G. Chen, Y. Guan, and W. Deng, "Study on aerodynamic drag reduction at tail of 400 km/h EMU with air suction-blowing combination," Machines **11**, 222 (2023).

[33] E. O. Shkvar, A. Jamea, S. J. E. J. C. Cai, and A. S. Kryzhanovskyi, "Effectiveness of blowing for improving the high-speed trains aerodynamics," Thermophys. Aeromech. **25**, 675 (2018).

[34] X. Liang, Z. Luo, X. Li, X. Xiong, and X. Zhang, "Drag reduction of high-speed trains via low-density gas injection," AIP Adv. **12**, 065115 (2022).

[35] C. Li, M. Liu, R. Chang, X. Wang, W. Liu, and H. Zhang, "Air pressure and comfort study of the high-speed train passing through the subway station," Sustainable Cities Soc. **81**, 103881 (2022).

[36] X. Xiong, L. Zhu, J. Zhang, A. Li, X. Li, and M. Tang, "Field measurements of the interior and exterior aerodynamic pressure induced by a metro train passing through a tunnel," Sustainable Cities Soc. **53**, 101928 (2020).

[37] H. Hemida, C. Baker, and G. Gao, "The calculation of train slipstreams using large-eddy simulation," Proc. Inst. Mech. Eng., Part F **228**, 25 (2014).

[38] Z. Li, M. Yang, S. Huang, and D. Zhou, "A new moving model test method for the measurement of aerodynamic drag coefficient of high-speed trains based on machine vision," Proc. Inst. Mech. Eng., Part F **232**, 1425 (2018).

[39] Z. Liu, D. Zhou, D. Soper, G. Chen, H. Hemida, Z. Guo, and X. Li, "Numerical investigation of the slipstream characteristics of a maglev train in a tunnel," Proc. Inst. Mech. Eng., Part F **237**, 179 (2023).

[40] Y. Fang, G. Li, L. Duan, Z. Han, and Y. Zhao, "Effect of surge motion on rotor aerodynamics and wake characteristics of a floating horizontal-axis wind turbine," Energy **218**, 119519 (2021).

[41] Z. Chen, T. Liu, W. Li, Z. Guo, and Y. Xia, "Aerodynamic performance and dynamic behaviors of a train passing through an elongated hillock region beside a windbreak under crosswinds and corresponding flow mitigation measures," J. Wind Eng. Ind. Aerodyn. **208**, 104434 (2021).

[42] Z.-W. Chen, E.-Z. Rui, T.-H. Liu, Y.-Q. Ni, X.-S. Huo, Y.-T. Xia, W.-H. Li, Z.-J. Guo, and L. Zhou, "Unsteady aerodynamic characteristics of a high-speed train induced by the sudden change of windbreak wall structure: A case study of the Xinjiang railway," Appl. Sci. **12**, 7217 (2022).

[43] Z.-W. Chen, G.-Z. Zeng, S. A. Hashmi, T.-H. Liu, L. Zhou, J. Zhang, and H. Hemida, "Impact of the windbreak transition on flow structures of the high-speed railway and mitigation using oblique structure and circular curve structure transition," Int. J. Numer. Methods Heat Fluid Flow **33**, 1354 (2023).

[44] S. Huang, Z-x Che, Z-w Li, Y-n Jiang, and Z-g Wang, "Influence of tunnel cross-sectional shape on surface pressure change induced by passing metro trains," Tunnelling Underground Space Technol. **106**, 103611 (2020).

[45] Y. Lu, T. Wang, C. Zhao, Y. Zhu, X. Jia, L. Zhang, F. Shi, and C. Jiang, "An efficient design method of indoor ventilation parameters for high-speed trains using improved proper orthogonal decomposition reconstruction," J. Build. Eng. **71**, 106600 (2023).

[46] C. D. Tan, D. Zhou, G. Chen, J. Sheridan, and S. Krajnovic, "Influences of marshalling length on the flow structure of a maglev train," Int. J. Heat Fluid Flow **85**, 108604 (2020).

[47] Z.-X. Che, S. Huang, Z.-W. Li, and Z.-W. Chen, "Aerodynamic drag reduction of high-speed maglev train based on air blowing/suction," J. Wind Eng. Ind. Aerodyn. **233**, 105321 (2023).

[48] J. Bell, D. Burton, M. Thompson, A. Herbst, and J. Sheridan, "Dynamics of trailing vortices in the wake of a generic high-speed train," J. Fluids Struct. **65**, 238 (2016).

[49] J. R. Bell, D. Burton, M. C. Thompson, A. H. Herbst, and J. Sheridan, "Moving model analysis of the slipstream and wake of a high-speed train," J. Wind Eng. Ind. Aerodyn. **136**, 127 (2015).

[50] H-q Tian, S. Huang, and M-z Yang, "Flow structure around high-speed train in open air," J. Cent. South Univ. **22**, 747 (2015).

[51] K. Xu, X. Su, R. Bensow, and S. Krajnovic, "Drag reduction of ship airflow using steady Coanda effect," Ocean Eng. **266**, 113051 (2022).

[52] S. Huang, H. Hemida, and M. Z. Yang, "Numerical calculation of the slipstream generated by a CRH2 high-speed train," Proc. Inst. Mech. Eng., Part F **230**, 103 (2016).

[53] D. Borgmann, A. Pande, J. C. Little, and R. Woszidlo, "Experimental study of discrete jet forcing for flow separation control on a wall mounted hump," 55th AIAA Aerospace Sciences Meeting, 9–13 January 2017, Grapevine, Texas (AIAA, 2017).

[54] A. Seifert, S. Eliahu, D. Greenblatt, and I. Wygnanski, "Use of piezoelectric actuators for airfoil separation control," AIAA J. **36**, 1535 (1998).